J Appl Electrochem (2009) 39:1545–1551
DOI 10.1007/s10800-009-9838-x

ORIGINAL PAPER

Electrochemical characteristics of boron doped polycrystalline diamond electrode sintered by high pressure and high temperature

J. B. Zang · Y. H. Wang · H. Huang · W. Q. Liu

Received: 28 August 2008 / Accepted: 9 February 2009 / Published online: 25 February 2009

Abstract The bulk B-doped polycrystalline diamond (PCD) electrode in this study was prepared by high-pressure, high-temperature (HPHT) technology. The PCD was sintered under HPHT conditions, using B-doped diamond powders and a metal catalyst as raw materials, then the metal solvent phase was dissolved by aqua regia. The morphology and composition of the PCD were investigated with a scanning electron microscope (SEM), X-ray diffraction (XRD), and energy dispersion spectrum (EDS). The results show that the sintered body possesses a polycrystalline structure with direct diamond–diamond bond and irregularly shaped pores of 1–10 μm distributed on the grain boundaries after the metal solvent phase was removed. The cyclic voltammogram and electrochemical impedance spectroscopy of this B-doped electrode have been investigated. The B-doped PCD electrode exhibits stable electrochemistry in a KCl support solution over a wide potential range. The quasi-reversible reaction occurs on the electrode for the $[Fe(CN)_6]^{3-/4-}$ couples. The electrode process combines the diffusion-controlled mass transport plus the kinetic process. The electrochemical impedance spectroscopy (EIS) analysis shows the porous structure characteristic of the PCD electrode.

Keywords High pressure · High temperature · Boron doped · Polycrystalline diamond · Porous electrode · Electrochemical

J. B. Zang · Y. H. Wang (✉) · H. Huang · W. Q. Liu
State Key Laboratory of Metastable Material Science & Technology, College of Material Science & Engineering, Yanshan University, Qinhuangdao 066004, People's Republic of China
e-mail: diamondzjb@163.com

1 Introduction

Conductive diamond film electrodes have received great attention in past decades due to their unique electrochemistry properties, such as wide potential window and low background current in aqueous or non-aqueous electrolytes; high chemical and electrochemical stabilities; and excellent corrosion stability, even in strong acidic media, etc. [1]. All of these properties make diamond electrodes well-suited for wide electrochemical applications in the electroanalysis [2–5] and electrosynthesis fields [6–8].

Boron doped diamond (BDD) film electrodes fabricated by chemical vapor deposition (CVD) techniques are the most widely studied and well reported in the literature [9–11]. However, a high surface area or porous electrode is required in some electrochemical fields such as electrochemical capacitors, electrocatalysis, electrochemical filters, and electrochemical treatment of waste water. Clearly, the CVD diamond film is not a competent material for these applications. To increase the double-layer capacitance, Fujishima et al. [12] fabricated nano-honeycomb diamond electrodes with a honeycomb-like array of deep, cylindrical pores with a high aspect ratio using oxygen plasma etching on CVD diamond film. The nano-honeycomb diamond electrodes exhibited high capacitance and a wide potential window. Swain et al. [13] recently proposed a new method to fabricate high-surface- area and conductive BDD electrodes by coating the insulated diamond powders with a conductive BDD layer using the CVD method and suggested the use of the conductive diamond powders as electrocatalystic support.

Compared with the CVD technique, the production of diamond powders by the HPHT method has already been proven to be a relatively cheap high-volume technology. Previous work in our research group has presented a

method to synthesize BDD crystals under the conditions of high pressure and high temperature using boron-doped graphite intercalation compounds (GICs) as carbon sources [14, 15]. We have also investigated the electrochemical behavior of BDD powder electrode in the neutral supporting electrolyte and the solution containing $K_3Fe(CN)_6$/$K_4Fe(CN)_6$ redox couple [16]. However, the complexity of packed powders on the morphology and the density makes the electrochemical results difficult to repeat exactly while using either the same electrode or different electrodes. Moreover, the inconvenience in the cleaning process also limits the application of the powder electrode.

In the present work, we fabricated a boron doped polycrystalline diamond by HPHT sintering and a porous structure formed by subsequent acid etching to remove the metal compositions, which acted as a solvent during the sintering process. This bulk and porous BDD polycrystalline can be applied as a novel diamond electrode, which has large surface area, long-term stability, and is easy to clean compared with the powder electrode. The electrochemical behavior of a synthetic diamond electrode was evaluated by the cyclic voltammetry (CV) and AC impendence measurements.

2 Experimental

2.1 Fabrication of B-doped PCD electrode

BDD crystals were synthesized by the HPHT method using H_3BO_3-GICs as carbon sources. The details were introduced in the references [14]. X-ray fluorescence results confirmed that the boron content in the diamond reached about 3.75×10^{20} cm^{-3}. The particles were compacted to powders finer than 20 μm and the packed powders' resistivity as measured by ohmmeter was 6.75 Ω cm. BDD powders were mixed with 15 wt% Fe–Co–B alloy powders (average grain size of 10 μm), which were chosen as a catalytic solvent and then put into the cylindrical graphite mould ($\varphi 6 \times 3$ mm). The packed graphite moulds were placed in the pyrophyllite high-pressure mould shown in Fig. 1. The high-pressure sintering process was performed at 1,450 °C and 6 GPa for 10 min on the cubic-type, high-pressure equipment. The obtained compacts were treated in boiled aqua regia for 12 h to remove the metal and the corresponding pores left inside the sintered body. XRD, EDS and SEM were used to investigate the composition and the morphology of the PCD. The porosity was measured by Archimedes' method. Thus, the prepared B-doped PCD sample was sealed into a silicone tube, the exposed end (the surface area was about 0.17 cm^2) was polished by diamond powders, and the opposite end was attached to a copper wire. The prepared B-doped PCD electrode was used as the working electrode in the following electrochemistry measurement.

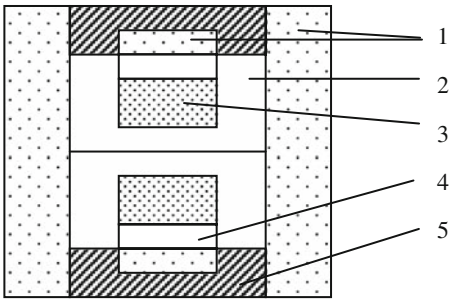

Fig. 1 High-pressure assembly: (1) Pyrophyllite, (2) Graphite mould, (3) Mixture of BDD powders and alloy powders, (4) Graphite plate, (5) Steel ring

2.2 Electrochemical measurement of B-doped PCD electrode

A CHI600A electrochemistry analyzer was used to perform the electrochemistry experiments. The CV and AC impedance measurements were carried out in a single-compartment, three-electrode system, which consisted of a B-doped PCD electrode as the working electrode, a saturated calomel electrode (SCE) reference electrode, and a platinum coil counter electrode. The CVs of the PCD electrodes in a solution of KCl containing $K_3Fe(CN)_6$/$K_4Fe(CN)_6$ were recorded. The scan rates were set as 0.01–1 V s^{-1}. The potential amplitude of the AC signal was kept as 5 mV and the measured frequency range was 10^{-2}–10^5 Hz in AC impedance experiments.

All solutions were prepared using reagent grade chemicals in doubly distilled water. The solutions were purged by N_2 prior to the electrochemical measurements. Ultrasonic cleaning was required for the PCD electrode when the electrolyte changed.

3 Results and discussion

3.1 Morphology and composition of synthetic B-doped PCD

Figure 2 shows the morphology of the PCD compact after high-pressure sintering (a) and then acid eroding (b), (c). The ternary alloy melted under high temperature and catalyzed the graphitation of the diamond surface, leading to diamond recrystallization and the formation of a polycrystalline structure with a direct diamond–diamond bond. Good bonding among diamond crystals is clearly exhibited in Fig. 2a. The metal phase dispersedly resides in the corner among diamond grains or intercrystallite boundaries. Pores form at the corresponding positions after the

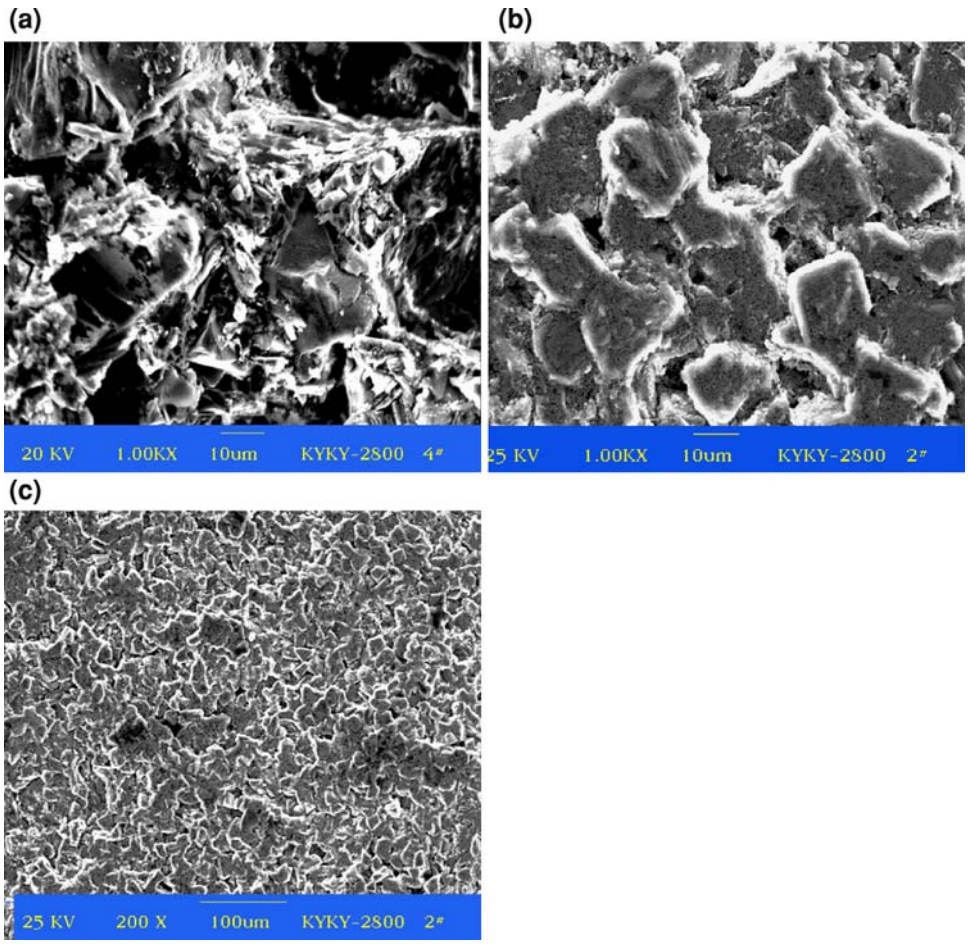

Fig. 2 Morphology of the sintered PCD (**a**), after acid eroding (**b**, **c**)

metal is removed by treating it in boiling aqua regia as shown in Fig. 2b. No metal phase was found in the XRD results (Fig. 3) and less than 5% metal inclusion was detected by EDS, as shown in Fig. 4. It is concluded that the metal has little effect on the conductivity of PCD. Indirect evidence suggests the change of PCD resistance from 1.5–5 to 15–120 Ω after acid eroding. The good conductivity of the sintered PCD arises from the contribution of the residual metal net and the higher resistance is due to B-doped PCD after the metal was removed. The irregular pores of 1–10 μm dispersed on grain boundaries, as shown in Fig. 2c, and the porosity was measured at 14 vol.%.

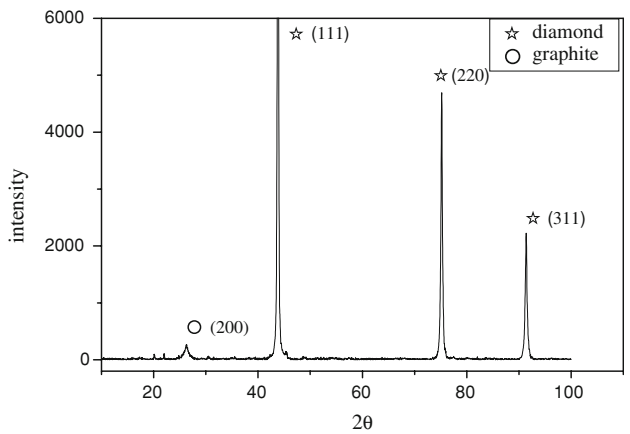

Fig. 3 XRD pattern of the PCD after acid eroding

3.2 Cyclic voltammetric characteristics of B-doped PCD electrode

Figure 5 shows a CV curve on the B-doped PCD electrode in the solution of 0.1 M KCl at a scan rate of 0.1 V s^{-1} over the potential range of −2–2.2 V. It exhibits a wide potential window that is the characteristic of BDD electrodes [17, 18]. The CV curves on B-doped PCD electrodes at different scan rates in 0.1 M KCl solutions containing 0.01 M $[Fe(CN)_6]^{3-/4-}$ redox couple are shown in Fig. 6. Well-defined, symmetric curves are seen with the peak separation ΔE_p of 103–224 mV vs. SCE, corresponding to the scan rate from 0.01 to 0.5 V s^{-1}. The $[Fe(CN)_6]^{3-/4-}$ redox reaction at the B-doped PCD electrode exhibits quasi-reversible electrochemical kinetics. The linear relationship between anodic peak current I_p and the square root

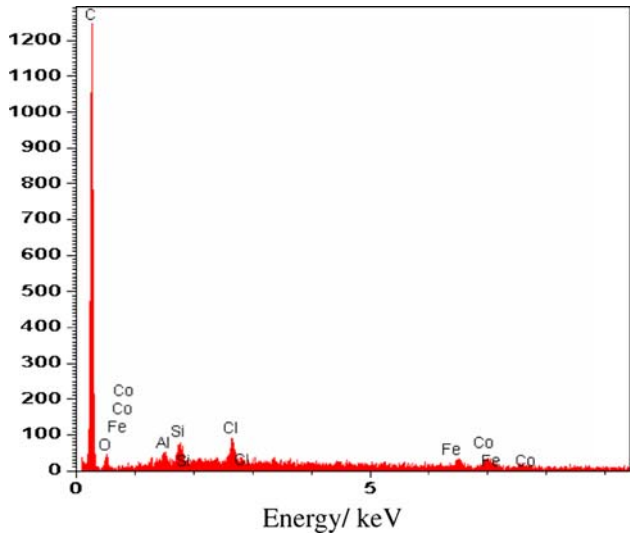

Fig. 4 EDS of the PCD after acid eroding

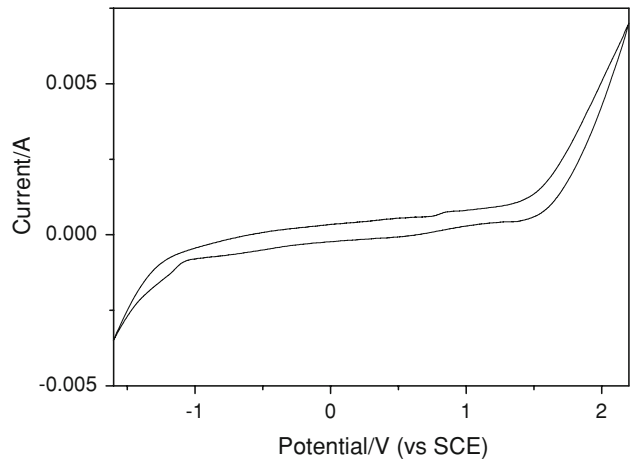

Fig. 5 CV curve on a B-doped PCD electrode in 0.1 M KCl at a scan rate of 0.1 V s^{-1}

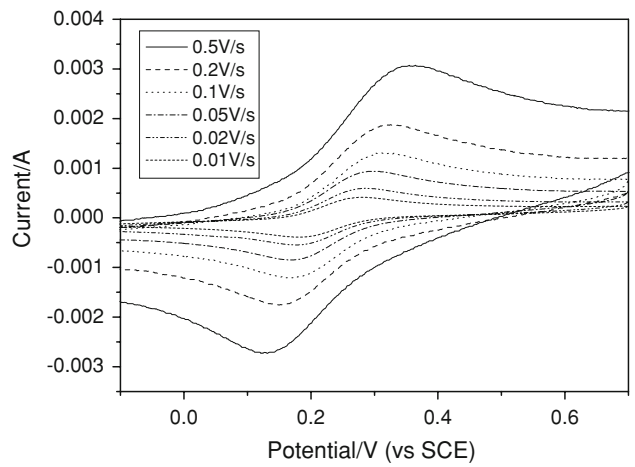

Fig. 6 CV curves on a B-doped PCD electrode in 0.1 M KCl +0.02 M $[Fe(CN)_6]^{3-/4-}$ at different scan rates

of scan rate $v^{1/2}$ (as shown in Fig. 7) at the scan rate of 0.01–0.1 V s^{-1} indicates a diffusion-controlled process at the electrode. At the higher scan rate, the peak current deviates from the linear relation with $v^{1/2}$, implying the inner surfaces of the pores are involved in the electrochemical reaction.

Figure 8 shows the CVs on the B-doped PCD electrode in 0.1 M KCl solutions containing $[Fe(CN)_6]^{3-/4-}$ redox couple of different concentrations. The peak current increases with the rising of the concentration of $[Fe(CN)_6]^{3-/4-}$ and the linear relationship is shown in the insert section.

3.3 EIS of B-doped PCD electrode

The further electrochemical information of the B-doped PCD electrode is obtained by employing EIS. Figure 9 shows the Nyquist plot on the B-doped PCD electrode in

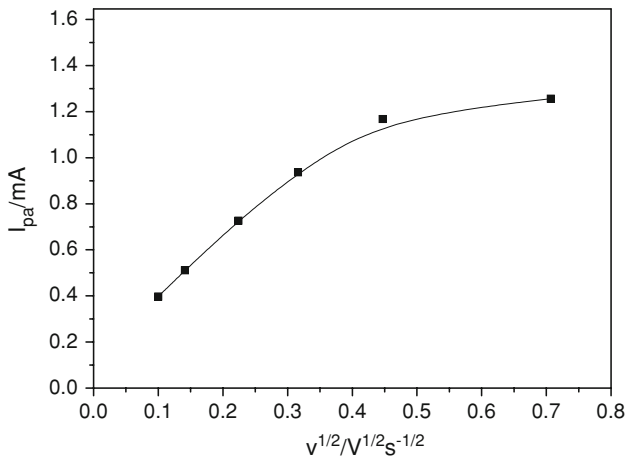

Fig. 7 Peak current vs. the square root of the scan rate

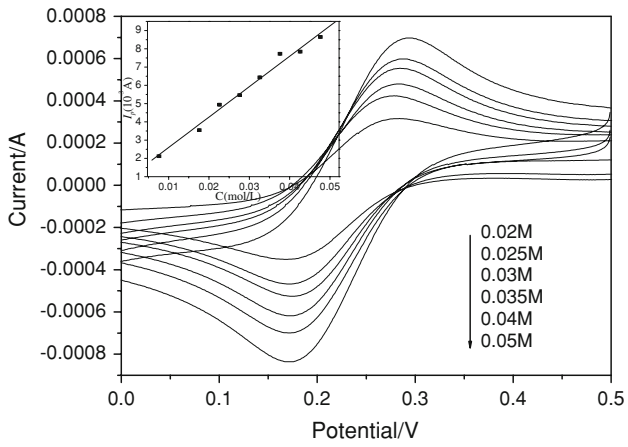

Fig. 8 CV curves on the B-doped PCD electrode in 0.1 M KCl containing $[Fe(CN)_6]^{3-/4-}$ of different concentrations at scan rates of 0.05 V s^{-1}. *Inset*: Peak current vs. $[Fe(CN)_6]^{3-/4-}$ concentration

0.1 M KCl electrolytes at the potential of 0 V vs. SCE. The frequency range is 10^{-1}–10^{5} Hz. The impedance spectrum in the absence of electro-active species presents two semicircle arcs, which can be described by a simple equivalent circuit consisting of two *RC* elements in a series, as shown in the insert of Fig. 9 [17]. The *RC* element corresponding to the high-frequency semicircle represents the impedance resulting from the resistance of the PCD electrode R_d in parallel with the capacitance C_d at the contact interface between the B-doped PCD electrode and the electrolyte solution. The depressed arc in the low-frequency region associates with the electric double layer on the inner surface of the pores, which can be expressed as R_cC_{dl} parallel circuit in the equivalent circuit. The charge transfer resistance inside the pores R_c increases distinctly and the inhomogeneous porous structure (sizes, shapes, and depths) leads to the frequency dispersion, so the double-layer capacitance C_{dl} is replaced by a constant phase element (CPE) [18–23] whose impedance is formulated by:

$$Z_{CPE} = (Y_0)^{-1}(j\omega)^{-\alpha} \quad (1)$$

where the constant Y_0 and the exponent α are frequency-independent and ω is the angular frequency. α is a correction factor related to the roughness of electrode surfaces, with values ranging between 0 and 1. Y_0 acts as a capacitance when $\alpha = 1$ and CPE is a pure resistance when $\alpha = 0$, if $\alpha = 0.5$, CPE is a pure Warburg impedance.

The solid line in Fig. 9 is simulated curve based on the equivalent circuit; the simulated parameters $R_d = 65 \pm 1\ \Omega$, $C_d = 2.45 \times 10^{-8} \pm 0.02$ F, and $R_c = 1{,}430 \pm 20\ \Omega$; and the parameters of CPE $\alpha = 0.68 \pm 0.003$ and $Y_0 = 1.45 \times 10^{-3} \pm 0.005\ F^{\alpha}\ \Omega^{\alpha-1}$. The calculated double-layer capacitance of the CPE element is 31.4 mF/cm^2. It is obvious that the double-layer capacitance resulting from the porous structure is far higher than C_{dl} of planar film electrode ($C_{dl} = 10\ \mu F\ cm^{-2}$) [12].

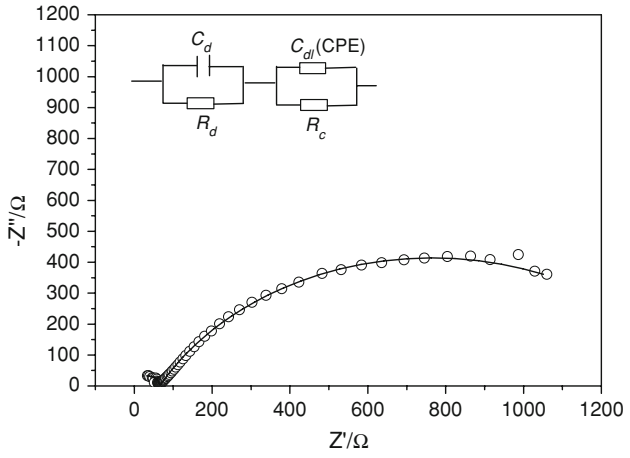

Fig. 9 Nyquist plot of the B-doped PCD electrode in 0.1 M KCl at the potential of 0 V. The *solid line* is the simulated curve calculated on the basis of the equivalent circuit shown in the inset

Figure 10 presents Nyquist plots on the B-doped PCD electrode in 0.1 M KCl containing 0.01 M $[Fe(CN)_6]^{3-/4-}$ redox couples at different applied potentials vs. SCE. The measured frequency range is from 10^5 to 10^{-2} Hz. A slight arc in the high frequency, which relates to the parallel R_dC_d element, connects with a straight line with a tilt angle of 33° followed by a depressed semicircle with different diameters, which is a characteristic of a porous electrode. The slope of the line, less than 45°, indicates the shape of the pores is not cylindrical and the inner surface is inhomogeneous [19]. The plots in the high- and medium-frequency parts are independent of the applied potentials, shown as the insert section in Fig. 10. The proposed equivalent circuit is shown in Fig. 11, in which CPE1 acts as a pseudo-Warburg impedance because the value of α (0.35–0.37) tends to be 0.5 [20]. The low-frequency

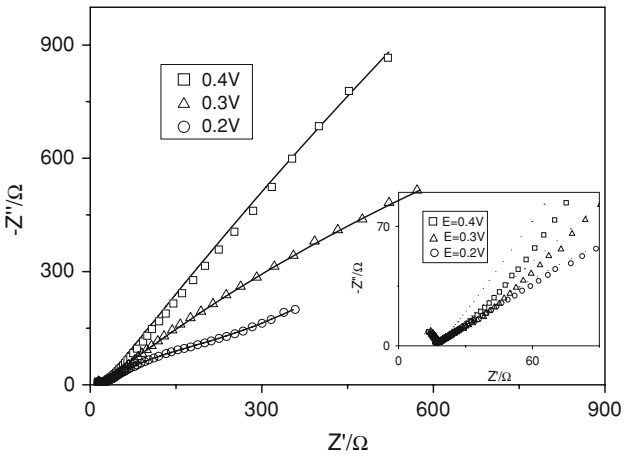

Fig. 10 Nyquist plots of the PCD electrode in 0.1 M KCl+0.01 M $[Fe(CN)_6]^{3-/4-}$ at the potential of 0.2, 0.3, 0.4 V. The *solid line* is the simulated curve calculated on the basis of the equivalent circuit in Fig. 11

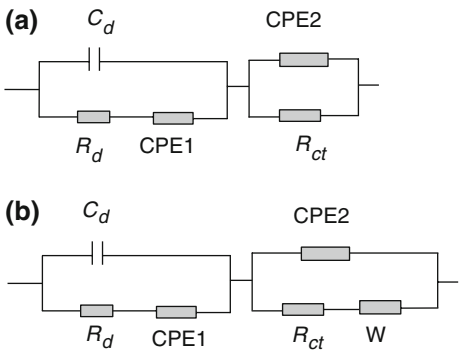

Fig. 11 Equivalent circuit of the reaction on the B-doped PCD electrode in 0.1 M KCl + 0.01 M $[Fe(CN)_6]^{3-/4-}$: **a** For $E > 0.3$ V or $E < 0.1$ V. **b** For $E = 0.1$–0.3 V

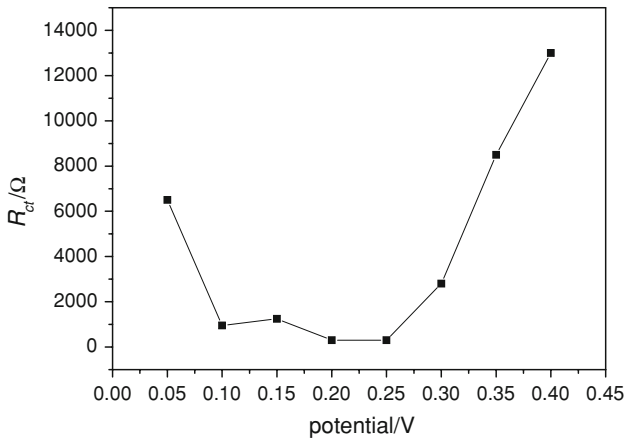

Fig. 12 Potential dependence of the value of R_{ct}

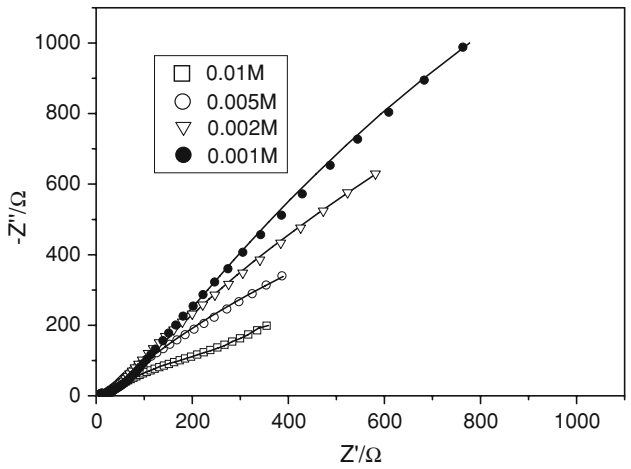

Fig. 13 Nyquist plots of the PCD electrode in 0.1 M KCl containing $[Fe(CN)_6]^{3-/4-}$ of different concentrations at the potential of 0.2 V. The solid line is the simulated curve calculated on the basis of the equivalent circuit in Fig. 11

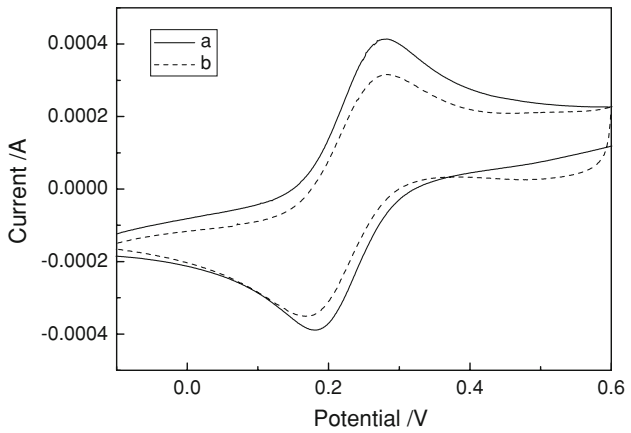

Fig. 14 CV curves on the fresh B-doped PCD electrode (**a**), and the electrode used for 6 months (**b**) in 0.1 M KCl containing 0.02 M $[Fe(CN)_6]^{3-/4-}$, v = 0.01 V s^{-1}

semicircle associates with the charge transfer inside the pores, and the inhomogeneity of the pores leads to the depressed arcs, which are also expressed as R_{ct}-CPE2 parallel circuit in the equivalent circuit, as shown in Fig. 11a. The charge transfer resistance R_{ct} corresponding to the diameter of the low-frequency semicircle increases dramatically when the applied potential deviates from the half peak potential (0.23 V) of the oxidation reaction. Figure 12 shows the potential dependence of the charge transfer resistance R_{ct}. Therefore it is concluded that the low-frequency arc relates to the electrode kinetics [23]. It is also worth noting that the impedance at 0.2 V exhibits a straight line following the arc in the low-frequency part, implying the ion diffusion process inside the pores, so a Warburg diffusion element W is added in the equivalent circuit (Fig. 11b). This originates from the limited pore depth and relatively large pore size (micrometer scale in Fig. 2), and the ions are liable to penetrate to the bottom of the pores and transfer charges with the inner surface of pores. The electrode process is diffusion plus kinetic control, which is consistent with the results in Sect. 3.2.

The solid line in Fig. 10 is a simulated curve based on the equivalent circuit in Fig. 11. ("a" is used as $E = 0.2$, 0.3 V and "b" is used as $E = 0.4$ V). The fitting parameters are listed in Table 1.

Figure 13 displays Nyquist plots of B-doped PCD electrode in 0.1 M KCl containing $[Fe(CN)_6]^{3-/4-}$ of different concentrations at the potential of 0.2 V. With the increases of the concentration the value of R_{ct} decreases,

Table 1 Fitting parameters used in the simulation in Fig. 10

E/V		0.2	0.3	0.4
R_d/Ω		16.0 ± 0.2	16.8 ± 0.2	15.8 ± 0.2
$C_d/\times 10^{-8}$ F		5.5 ± 0.5	5.5 ± 0.5	5.5 ± 0.5
CPE1	$Y_{01}/F^{\alpha}\ \Omega^{\alpha-1}$	0.015 ± 0.001	0.010 ± 0.001	0.0091 ± 0.0005
	α_1	0.35 ± 0.005	0.35 ± 0.005	0.35 ± 0.005
$R_{ct}/\times 10^3\ \Omega$		0.32 ± 0.02	4.3 ± 0.1	15.85 ± 0.25
CPE2	$Y_{02}/\times 10^{-3}\ F^{\alpha}\ \Omega^{\alpha-1}$	2.0 ± 0.1	2.0 ± 0.1	2.1 ± 0.1
	α_2	0.55 ± 0.005	0.61 ± 0.005	0.76 ± 0.01

because R_{ct} is inversely proportional to the exchange current that depends on the redox couple concentration.

3.4 Stability of B-doped PCD electrode

The sintered polycrystalline structure has a far higher bond strength than the packed powders, so the PCD electrode has higher morphology stability. Figure 14 shows the CV curve on the PCD electrode in 0.1 M KCl containing 0.02 M $[Fe(CN)_6]^{3-/4-}$ after the electrode has been used for 6 months (the dash line). The slight decrease of the peak current suggests the electrode still has high electrochemical activity after long-term use. Almost overlapped Nyquist plots and SEM results (not shown here) also confirm that little structure and morphology changes occur in the PCD electrode. This implies the long life of the B-doped PCD electrode.

4 Conclusion

A high boron doped polycrystalline diamond was synthesized by high-pressure technology. The porous PCD with a diamond–diamond bond was obtained after removing the metal phase by acid etching. Irregularly shaped pores of 1–10 μm dispersively distributed on grain boundaries. The synthetic B-doped PCD electrode exhibits stable electrochemistry in KCl support solution over a wide potential range. For the $[Fe(CN)_6]^{3-/4-}$ couples, the B-doped PCD electrode reaction process is quasi-reversible. The electrode process is the diffusion-controlled mass transport plus the kinetic process. EIS analysis shows the porous structure characteristic of the PCD electrode. The high double layer capacitance resulting from the porous structure makes this B-doped PCD electrode probable suitable for application in capacitors. The high stability of the electrode implies the electrode has a long life.

Acknowledgements The authors acknowledge the support of the Fok Ying Tung Education Foundation (No. 91049), the Hebei Provincial Natural Science Foundation of China (No. E2004000220), and the National Natural Science Foundation of China (No. 50872119).

References

1. Fujishima A, Einaga Y, Rao TN, Tryk DA (2005) Diamond electrochemistry. Elsevier, Amsterdam
2. Einaga Y, Sato R, Olivia H et al (2004) Electrochim Acta 49:3989
3. Rao TN, Fujishima A (2000) Diam Relat Mater 9:384
4. Boonsong K, Chuanuwatanakul S, Wangfuengkanagul N et al (2005) Sens Actuators B 108:627
5. Park J, Show Y, Quaiserova V et al (2005) J Electroanal Chem 583:56
6. Serrano K, Michaud PA, Comninellis C et al (2002) Electrochim Acta 48:431
7. Wadhawan JD, Del Campo FJ, Compton RG et al (2001) J Electroanal Chem 507:135
8. Panizza M, Cerisola G (2005) Electrochim Acta 51:191
9. Ferreira NG, Silva LLG, Corat EJ et al (2002) Diam Relat Mater 11:1523
10. Duo I, Levy-Clement C, Fujishima A, Comninellisi C (2004) J Appl Electrochem 34:935
11. Ferro S, Battisti AD (2002) Electrochim Acta 47:1641
12. Honda K, Yoshimura M, Uchikado R et al (2002) Electrochim Acta 47:4373
13. Fischer AE, Swain GM (2005) J Electrochem Soc 152:B369
14. Zang JB, Wang YH, Huang H (2004) Key Eng Mater 259–260:42
15. Zang JB, Wang YH, Zhang XM et al (2002) J Mater Process Technol 129:454
16. Zang JB, Wang YH, Huang H et al (2007) Electrochim Acta 52:4398
17. Denisenko A, Pietzka C, Romanyuk A et al (2008) J Appl Phys 103:014904
18. Song HK, Hwang HY, Lee KH et al (2000) Electrochim Acta 45:4421
19. Hasbach A, Retter U, Siegler K et al (2004) J Electroanal Chem 561:29
20. Ibris N, Mirza-Rosca JC, Santana A (2002) J Solid State Electrochem 6:119
21. Chen WC, Wen TC (2003) Electrochim Acta 48:641
22. Nakahara H, Yoon SY, Piao T et al (2006) J Power Sources 158:591
23. Lasia A (2001) J Electroanal Chem 500:30